JGR Solid Earth

Key Points:

- New Vp, Vs, and Vp/Vs models for Southern California are derived from 20 years of seismic data with a recently developed tomography method
- Sharper images of fault-zone structures are revealed by the relocated earthquakes
- The depth-averaged Vp/Vs is higher than 1.77 in top 3 km, reaches a minimum of about 1.73 around 10 km, and increases again at greater depth

Correspondence to:

H. Fang,
fanghj23@mail.sysu.edu.cn

Author Contributions:

Formal analysis: Hongjian Fang
Funding acquisition: Yehuda Ben-Zion
Methodology: Malcolm C. A. White
Supervision: Yehuda Ben-Zion
Validation: Yang Lu
Writing – original draft: Hongjian Fang
Writing – review & editing: Malcolm C. A. White, Yang Lu, Yehuda Ben-Zion

Seismic Traveltime Tomography of Southern California Using Poisson-Voronoi Cells and 20 Years of Data

Hongjian Fang[1,2], Malcolm C. A. White[3], Yang Lu[4], and Yehuda Ben-Zion[5,6]

[1]School of Earth Sciences and Engineering, Sun Yat-sen University, Guangzhou, China, [2]Southern Marine Science and Engineering Guangdong Laboratory (Zhuhai), Zhuhai, China, [3]Department of Earth, Atmospheric and Planetary Sciences, Massachusetts Institute of Technology, Cambridge, MA, USA, [4]Department of Meteorology and Geophysics, University of Vienna, Wien, Austria, [5]Department of Earth Sciences, University of Southern California, Los Angeles, CA, USA, [6]Southern California Earthquake Center, University of Southern California, Los Angeles, CA, USA

Abstract We derive new, 3D, isotropic models of seismic compressional and shear wavespeeds, Vp and Vs, respectively, their ratio, Vp/Vs, and a catalog of relocated earthquakes for Southern California from more than 10 million P- and S-wave arrivals associated with over 0.3 million earthquakes that occurred between 2000 and 2020. We augment high-quality analyst-reviewed phase arrival picks from the Southern California Earthquake Data Center with S-wave arrival picks obtained with an automated algorithm, and we derive new wavespeed models via traveltime tomography formulated using Poisson-Voronoi cells (Fang et al., 2020, https://doi.org/10.1785/0220190141). The results contribute to improved regional wavespeed models, particularly the Vp/Vs model, and absolute event locations. The obtained models correlate well with regional geological features and yield more accurate synthetic waveforms than other regional models do for waves with periods shorter than 5 s in much of the modeled region. The derived event catalog exhibits tighter spatial clustering than the standard regional catalog, thereby helping to characterize subsurface features of major faults. The regional 1D averaged Vp/Vs ratio shows high values at shallow depths, decreases to a minimum at about 10 km, then increases again at greater depths below 15 km. Deep seismicity correlates well with regions of Vp/Vs ratio lower than 1.75, which may indicate an increased brittle-to-ductile transition depth with an important influence on crustal mechanics. The new wavespeed models and seismic catalog can be useful for various studies including analyses of seismicity patterns and simulations of crustal deformation and ground motion.

Plain Language Summary Motion along the tectonic plate boundary between the Pacific and North American plates is deforming the Earth's crust in Southern California and causing ongoing seismicity including numerous micro earthquakes not felt by humans. These earthquakes alter the physical properties of the crustal rocks that host them. In this study, we compile observations from over 0.3 million earthquakes in Southern California to construct new 3D models of the elastic properties of the crust, and to improve earthquake locations. The results show significant lateral and depth variations of seismic wavespeed consistent overall with previous studies. Earthquakes deeper than 15 km tend to concentrate in regions with low values of the elastic parameter Poisson's ratio. The models show that earthquakes in the Eastern California Shear Zone—a broad zone of distributed crustal deformation east of the main plate boundary—occur at unusually shallow depths, possibly as a result of weakened crust between 10 and 15 km depth. This zone of weak crust may also be partially responsible for the networks of closely spaced, perpendicular faults found in the area. A section in the central part of the San Jacinto fault with very few earthquakes may be a favorable site for a future large earthquake.

1. Introduction

Models of compressional wavespeed Vp, shear wavespeed Vs, and Vp/Vs ratio, which is closely related to Poisson's ratio, are of great importance for many studies of seismotectonic processes, earthquake dynamics, hazard assessment and more. In the past several decades, considerable effort has been directed toward deriving such models in Southern California (SoCal) with multiple data sets and techniques. These include waveform inversions of earthquake data (Tape et al., 2009, 2010), waveform inversions of earthquake data and empirical Green's functions estimated using ambient-noise cross correlation (Lee et al., 2014), joint inversion of body-wave travel times and surface-wave dispersion measurements (Fang et al., 2016, 2019), joint inversion of surface-wave dispersion measurements, H/V ratio measurements and receiver functions (Berg et al., 2018, 2021), and various additional inversions using body waves and

noise correlation data (Allam & Ben-Zion, 2012; Barak et al., 2015; Lin et al., 2007; Qiu et al., 2019; Tong, 2021; Zigone et al., 2015). The tomographic results of Tape et al. (2010) combined with basin structures based on industry data form the community velocity model CVMH15.1 (Shaw et al., 2015) of the Southern California Earthquake Center (SCEC). Another SCEC community velocity model CVMS4.26 is based on the waveform tomography results of Lee et al. (2014). Additional refinements of regional models for SoCal are described in Wang et al. (2018). A recent validation study comparing the performance of the CVMH15.1, CVMS4.26, and Berg et al. (2018) Vp and Vs models shows that they have variable performance for different phases, frequency ranges, and crustal sections (Lu & Ben-Zion, 2022). In addition, none of the existing regional models is likely to provide reliable Vp/Vs ratios, because they derive Vp and Vs models using data with different sensitivity to Vp and Vs, along with different a priori information, approximations, and regularizations of the inverse problem.

In the present study, we derive new, self-consistent Vp, Vs, and Vp/Vs regional models for SoCal, using a large amount of earthquake travel time data and a recent methodology that reduces the number of assumptions involved in obtaining tomographic images. We recompile P- and S-wave first arrivals from the SCEC Data Center (SCEDC; Southern California Earthquake Center, 2013), and augment these data with additional S-wave arrival times obtained using an automated picker. We then employ a recently developed method that uses flexible parameterization based on Poisson Voronoi cells and is capable of handling very large data sets with fewer subjective regularizations (Fang et al., 2020). We improve the original method by adaptively increasing cell density in regions with higher data coverage, thus increasing the spatial resolution where data allow. In addition, we estimate model uncertainty due to data error using a bootstrapping-like technique, which is implicit in our tomographic method.

In the following sections, we first introduce the data used in the tomographic study, followed by a brief description of the inversion technique using the Poisson Voronoi cells. We then present various features of the obtained results, with an emphasis on the Vp/Vs model, which is likely better constrained than previous models, and relocated seismicity using the obtained wavespeed models. We perform a comparative validation of the models using waveform simulation and calculate model uncertainties. The obtained models are shown to outperform other regional models in a large portion of SoCal in terms of fitting short-period body and surface waves. Considering the relations between the seismicity and the wavespeed models, we observe that the depth distribution of earthquakes is anti-correlated with the depth-averaged Vp/Vs ratio. Most seismicity deeper than 15 km is found to occur in regions with Vp/Vs ratio <1.75, which might correspond to deeper brittle to ductile transition and higher overall seismic potential.
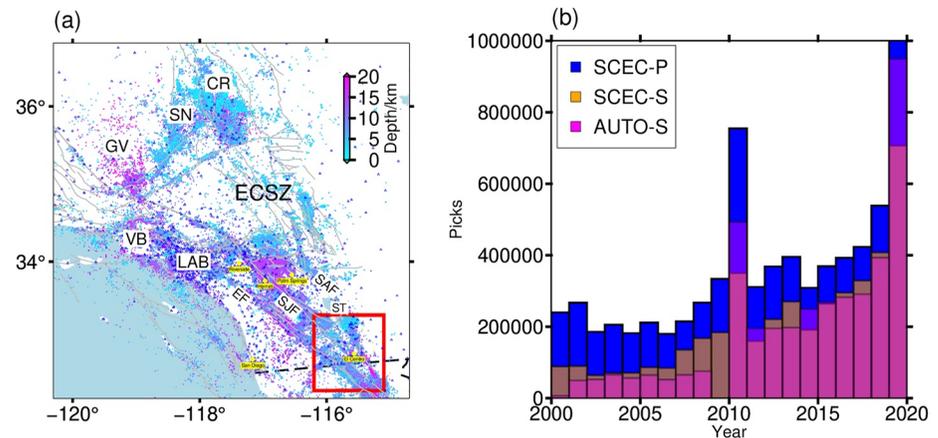
2. Data and Methods

2.1. Catalog Data Used in the Inversion

We download seismic P- and S-wave phase arrival data for events between 1 January 2000 and 31 December 2019 from the SCEC Data Center. We currently exclude arrivals with epicentral distance larger than 120 km to mitigate the multi-pathing effect of Pg/Sg and Pn/Sn phases. The data set initially comprises 7,254,222 and 4,232,529 analyst-reviewed P- and S-wave arrivals, respectively, which are associated with 345,216 earthquakes (Figure 1a). We discard arrivals with residual greater than 2 s compared to synthetic arrival times computed using the Modified Hadley-Kanamori 1D velocity model (HK1D, Hauksson & Shearer, 2005), and we subsequently discard events associated with fewer than 10 arrivals with acceptable residuals. The quantity of P-wave arrivals exceeds that of S-wave arrivals by 3,021,693, because determining S-wave onsets is often difficult due to interference with the coda of the preceding P waves.

To increase the number of S-wave picks, which are essential for resolving robust Vp/Vs ratio models (Kennett et al., 1998; Fang et al., 2019), we implement an automated picking algorithm (Figure 2) based on the Akaike Information Criterion (AIC; Akaike, 1974) implemented via Equation 1
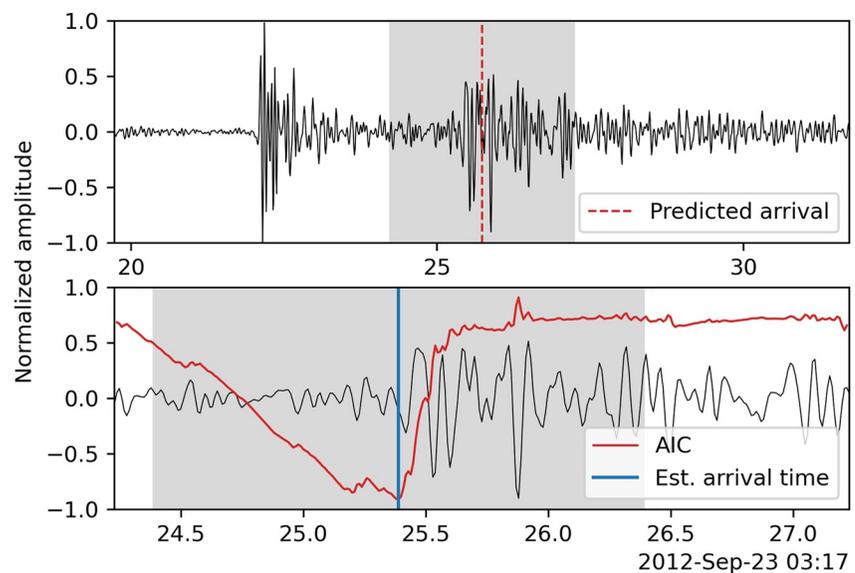
$$i^* = \arg\min_i \left(i \log \left(\text{var} \left(s \left[0 : i \right] \right) \right) + (n - i) \log \left(\text{var} \left(s \left[i : n \right] \right) \right) \right) \tag{1}$$

in which s is a length-n seismogram, i is a sample index, and $s[a : b]$ indicates the series of samples from s with indices greater than or equal to a and less than b. Our methodology follows previous work by, for example, Simon et al. (2020), and we refer readers to their paper for a more comprehensive analysis of AIC-based phase picking.

Figure 1. (a) Station (blue triangles) distribution in the study region. Gray lines indicate the fault traces. The red box shows the regions in Figure 4. SAF, San Andreas fault; SJF, San Jacinto fault; EF: Elsinore fault; ST, Salton Trough; LAB, Los Angeles Basin; VB, Vantori Basin; ECSZ, East California Shear Zone; GV, Great Valley; SN, Sierra Nevada; CR, Coso Range. (b) Histograms of P and S arrivals from the year 2000–2020 in the SCEDC augmented by automatic picking of S arrivals.

First, we download event-segmented waveforms for each event from SCEC Data Center using their Seismogram Transfer Program. Then, we (a) extract a 3 s window of three-component (3C) data, centered on the predicted arrival time computed using PyKonal (White et al., 2020) and the HK1D model, (b) bandpass filter waveforms between 1 and 20 Hz, (c) compute the AIC (e.g., Simon et al., 2020; White et al., 2021) for extracted, filtered waveforms (Equation 1), (d) register the time of the global minimum of the AIC for each component as a candidate S arrival, (e) compute the signal-to-noise ratio (SNR) for each candidate arrival using a 2 s window centered on the arrival, and (f) select the candidate arrival for each event-station pair from the component with the highest SNR as the automated S pick. We further discard automated picks with SNR less than 5, and, when both manual and automated picks are available for a given event, we discard the automated pick. In the final

Figure 2. Illustration of the Akaike Information Criterion (AIC) method used to augment the S-wave data set. The upper panel shows normalized, horizontal-component waveforms (HHE) for station AZ.BZN. The translucent gray area indicates the three-second window centered on the predicted arrival time (vertical, red, dashed line) that is used for picking. The lower panel indicates three-second window of data indicated in the upper panel with the arrival time (solid, vertical, blue line) estimated using the AIC (solid, red curve). The translucent gray area indicates the two-second window that used to compute the SNR.

analysis, we augment the analyst-reviewed data set with 2,941,667 automated S picks to obtain a data set with 7,174,196 S-wave picks, which is comparable to the number of P-wave picks (Figure 1b). The automated picks for events that also have analyst picks have RMS residual (difference between automated and analyst picks) of 0.1 s (Figure S1a in Supporting Information S1) and the Wadati diagram of S-P times versus P traveltimes with S arrival times from automatic picking and P arrival times from SCEC Data Center shows linear correlation (Figure S1b in Supporting Information S1), indicating again the robustness of our automatic picking. Additionally, we manually review a small subset (on the order of a few hundred) of the complementary, automated S-wave picks to verify their quality.

The final data set has comparable raypath coverage for P- and S-waves, which is critical for constraining the Vp/Vs model. This in turn helps to constrain, in concert with the Vp and Vs models, crustal lithology, porosity and fluid saturation, partial melting, and rock damage in fault zones.

2.2. Traveltime Tomography Based on Poisson-Voronoi Cell Projections
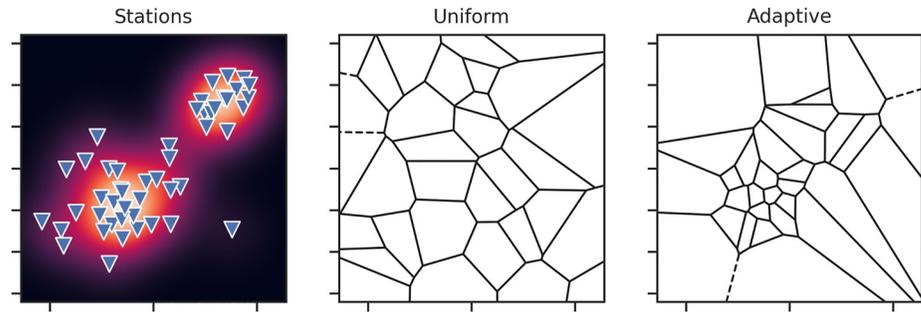
In this subsection, we briefly introduce key ideas behind the formulation of the tomographic problem based on Poisson-Voronoi cell subspace projections (see Fang et al., 2020, for a comprehensive treatment). We discuss in greater detail changes that we make in this study to the original algorithm to improve data selection and adaptively refine model resolution where possible.

The main benefit of the traveltime tomography method introduced by Fang et al. (2020) and applied in this study is that it stabilizes the inverse problem without explicit, subjective regularizations, such as damping and smoothing. Instead, the inverse problem is stabilized by averaging the solutions to multiple smaller subproblems, each with low dimensionality (i.e., relatively few unknowns to be solved for). Individual subproblems are constructed by projecting the high-dimensional model space into a lower-dimensional subspace randomly generated using Voronoi cells. Because only a subset of data is needed to constrain these low-dimensional subspace models, each one can be constrained using a different random subset of the data. The low-dimensional models can be projected back into the original high-dimensional model space and averaged to obtain a stable, final model. In addition to stabilizing the inverse problem by averaging solutions to multiple random realizations of low-dimensional subproblems, input data can be effectively homogenized (i.e., the distribution of raypaths) by weighted sampling with appropriately defined weights and model variance (i.e., sensitivity to data sampling) can be derived from the distribution of solutions.

The randomized subspace projections in Fang et al. (2020) were computationally inefficient (in terms of RAM and CPU use) because they were computed using matrix multiplication, which has $\mathcal{O}\left(n^3\right)$ computational complexity when performed naively for two $n \times n$ matrices, although can be improved when the matrices are sparse. In this study, we optimize the subspace projections by directly projecting each raypath into its subspace representation (i.e., path length through each Voronoi cell), following the approach of Sambridge and Guðmundsson (1998). Raypaths are computed using PyKonal (White et al., 2020). Optimizing the algorithm in this way is essential for analyzing a data set of the size considered in this study.

To mitigate the effect of spatially clustered events, which are ubiquitous in virtually all seismically active regions, including southern California (e.g., Zaliapin & Ben-Zion, 2013, 2021), and may dominate the inversion process, Fang et al. (2020) proposed weighted random data sampling to homogenize the event distribution for each subproblem. The probability of events used in the inversion is proportional to the number of events in a certain block. This, however, leads to some events which are not within event clusters being sampled many times while leaving others unsampled. Here, we propose a hierarchical sampling strategy comprising three weighting schemes, which are used sequentially to resolve structural features at various scales starting with the largest scale features.

The first weighting scheme, intended to constrain large-scale features, draws samples proportional to weights $w_i \equiv P^{-1}\left(\theta_i, \phi_i, z_i, \psi_i, \Delta_i\right)$, where θ_i, ϕ_i, and z_i are the latitude, longitude, and depth of the event associated with the ith ray, ψ_i and Δ_i are the event-to-station azimuth and distance, respectively, and $P\left(\cdot\right)$ is a 5-D kernel density estimate of the probability of randomly sampling a ray with those parameters. The kernel $P\left(\cdot\right)$ is estimated as in White et al. (2021). For this weighting scheme $w_i \to 0$ as $P\left(\cdot\right) \to \infty$ and, thus, dramatically reduces the number of samples drawn from highly clustered events. This maximizes the homogeneity of raypath coverage, helping to resolve large-scale features.

Figure 3. Schematic demonstration of adaptive cell refinement: (a) Stations (inverted, blue triangles) and kernel density estimate for station distribution (background color), (b) uniformly distributed Voronoi cells, and (c) adaptively distributed Voronoi cells with centers sampled from kernel density estimate in (a).

In subsequent iterations, samples are drawn proportional to weights $w_i \equiv e^{-P(\theta_i, \phi_i, z_i, \psi_i, \Delta_i)}$. This weighting scheme is bounded and thus allows greater sampling of clustered events, which helps to resolve intermediate-scale structures. Similar to White et al. (2021), after each wavespeed update, we relocate each event individually with a non-linear relocation algorithm based on Differential Evolution (Storn & Price, 1997). In the final iterations, samples are drawn with uniform probability. Event clusters dominate the inversion at this stage and help to resolve fine-scale features as the data permit (see Figure S2 in Supporting Information S1 for an example of ray distribution for a certain realization at different stages.).

In addition, we adaptively refine the distribution of the (latitude and longitude coordinates of) Voronoi cell centers such that the cell density mirrors the station density (Figure 3), similar to the refinement implemented by White et al. (2021). In contradistinction to the refinement in White et al. (2021), we distribute the depth coordinates of Voronoi cell centers uniformly. By combining hierarchical sampling and local refinement of Voronoi cells, we mitigate the effects of event and station clusters to obtain a model which has multi-scale features resolved by the heterogeneous data distribution.
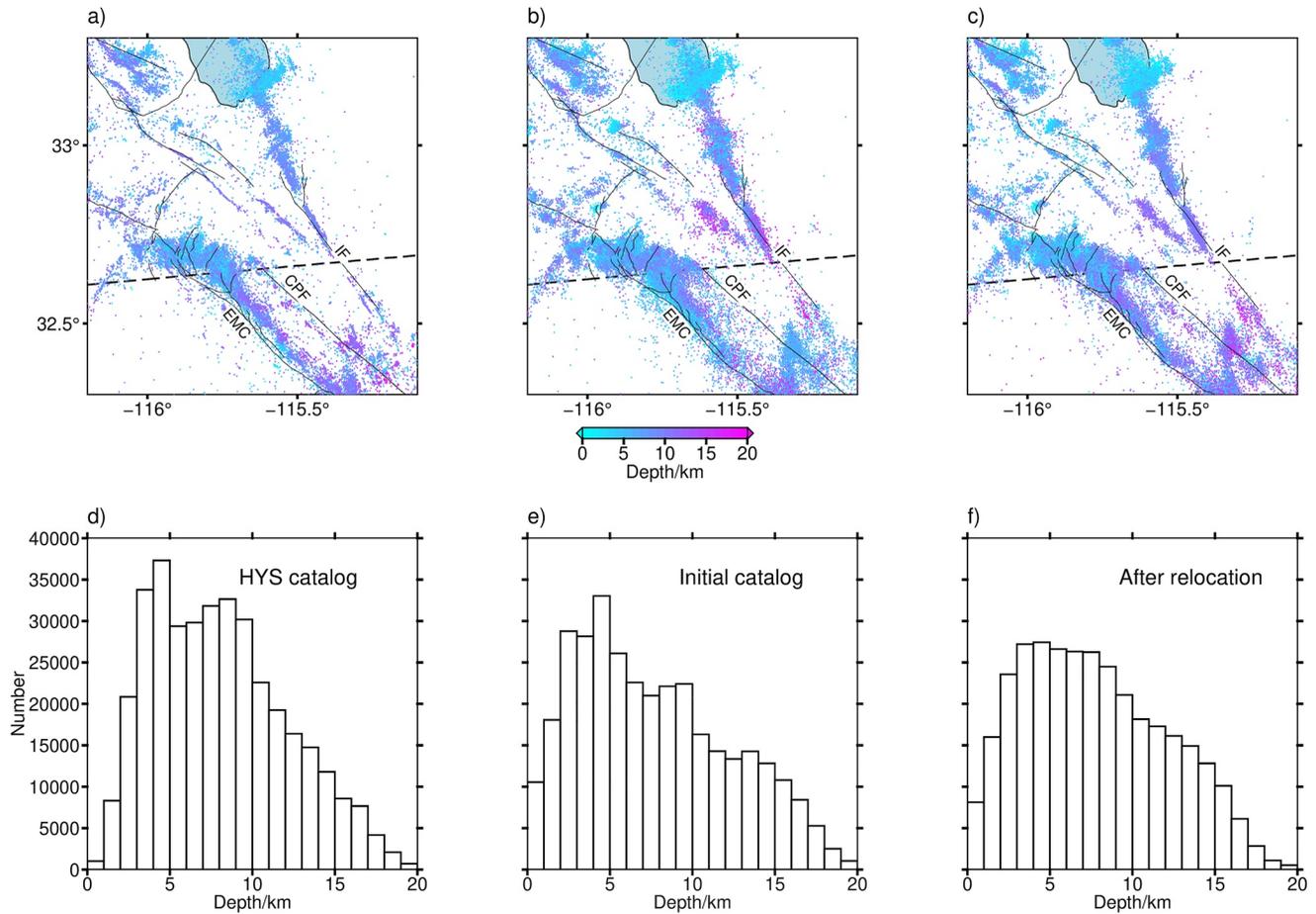
We obtain the relocated seismicity which consists of 344,650 events and final wavespeed models after six iterations; the standard deviation of residual drops from 0.23 to 0.20 s and 0.39 to 0.34 s for P- and S-wave arrivals, respectively (Figure S3 in Supporting Information S1).

3. Results

We discretize our model using a grid interval of about 3.0 km in horizontal directions and 1.0 km in vertical direction. The PyKonal software for the hybrid fast marching method (White et al., 2020) is used to calculate the traveltimes and raypaths between different event and stations pairs. We choose 1,000 events based on the probability density function of the event distribution for each realization, and 100 realizations for each iteration, which is sufficient to ensure stability and sufficient data sampling (Fang et al., 2020). We take the depth-averaged 1D version of the CVMS4.26 as our initial model because it has been shown to fit observed data better (Xiong et al., 2021). After each model update, we also relocate the events using PyKonal and Differential Evolution (Storn & Price, 1997), which is a non-linear, stochastic, global-search algorithm.

3.1. Relocated Seismicity

Large-scale spatial seismicity patterns of relocated events are generally similar to the initial event locations from the standard catalog, and improvements can be seen at finer scales (Figure 4) and regions with sparse station coverage usually show large variations (Figure S4 in Supporting Information S1). For example, south of the Salton Trough (ST), seismicity becomes more clustered along fault traces (Figures 4b and 4c) after relocation, although not as sharp as in Hauksson et al. (2012) where differential traveltimes are used for double-difference relocation and events not belonging to clusters are removed (Figure 4a). The locations near the Cerro Prieto fault (CPF) fault are especially clear with clustered seismicity after relocation (Figures 4b and 4c). The relocated catalog also exhibits a trend of deepening seismicity from the SE tip of ST to the SE end of the Imperial fault
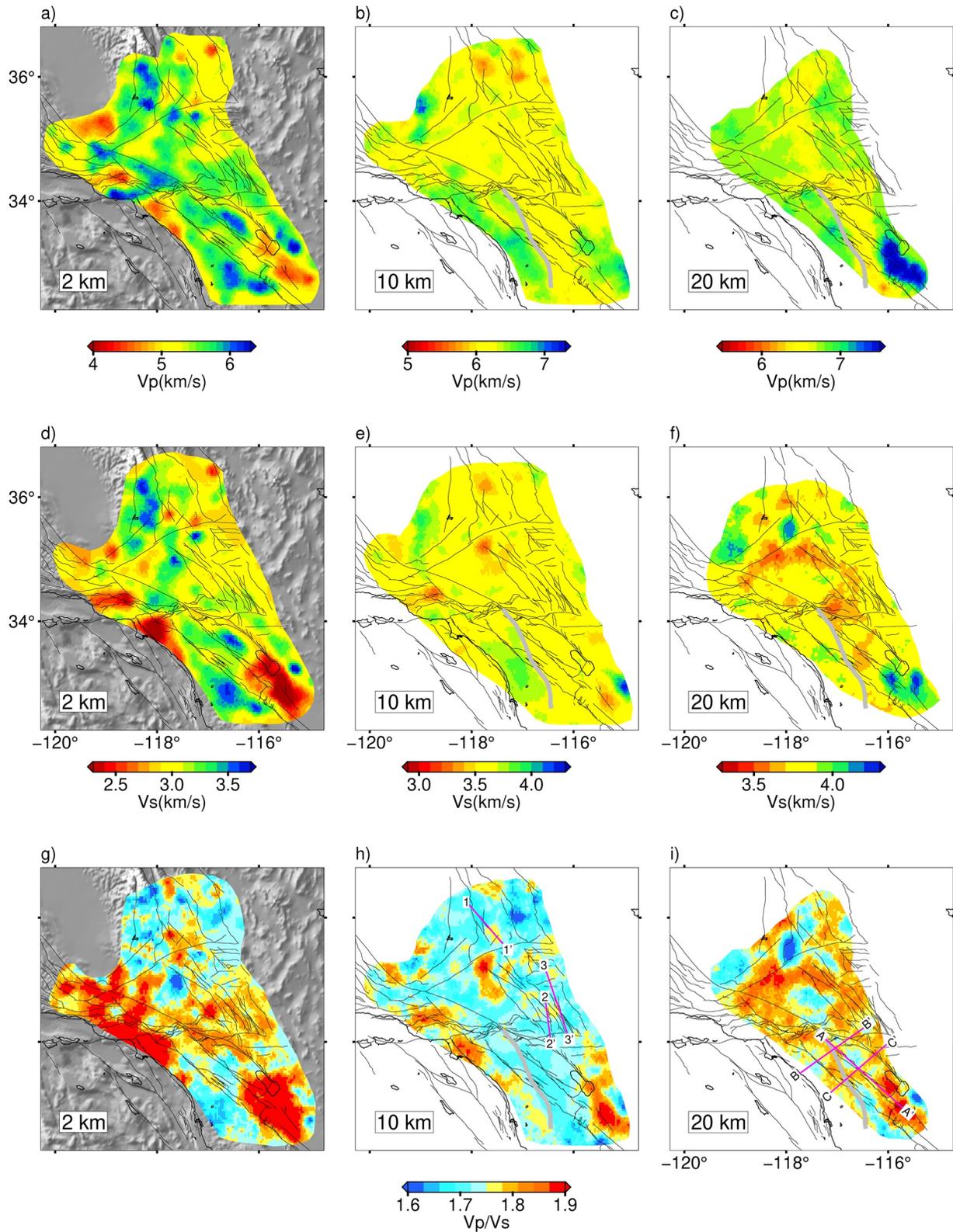
Figure 4. Comparison of events distribution in a small region to the south of Salton Trough (the location is indicated in Figure 1a) among (a) the Hauksson et al. (2012) catalog, (b) initial catalog from SCEDC, and (c) after relocation and (d–f) their corresponding depth distribution. IF, Imperial fault; CPF, Cerro Prieto fault; EMC, 2010 El Mayor-Cucapah rupture.

(IF) fault, which might be related to the ongoing rifting process in this region (Han et al., 2016). In addition, the cross-cutting seismicity pattern near the SE tip of the ST exhibits an L shape after relocation. The depth distribution of all events after relocation becomes smoother with most events in the range of 3–15 km (Figures 4d, 4e and 4f). The gradual tapering of seismicity with depth is consistent with the observed spatial variations of the Moho depth (Ozakin & Ben-Zion, 2015; Zhu & Kanamori, 2000) and heat flow (Blackwell & Richards, 2004) in the area.

3.2. 3D Wavespeed Models

The obtained wavespeed models are generally consistent with previous imaging results in SoCal, with significant low-wavespeed anomalies along the southern San Andreas fault related to damage zones in both Vp and Vs models at shallow depth above 5 km (Figure 5). Prominent basins, such as the Los Angeles basin, Ventura Basin, and the ST are associated with sedimentary geology and, therefore, low-wavespeed anomalies and high Vp/Vs ratio, in agreement with high H/V measurements (Muir & Tsai, 2017). Large wavespeed contrasts can be seen across faults, such as the NE part of San Jacinto fault (SJF) and the western segment of the Garlock fault. High-wavespeed anomalies at shallow depth are mostly associated with igneous rocks, which are primarily located in the Peninsular and Sierra Nevada mountain ranges. The amplitude of heterogeneities becomes smaller in the middle crust (at about 10 km depth). However, there is a clear contrast across the Peninsular Range Compositional Boundary (PRCB; Langenheim et al., 2004) with high Vp and Vs anomalies to the west corresponding to oceanic mafic rocks and low wavespeed felsic rocks to the east. The Peninsular Range Compositional Boundary (PRCB) is not clearly shown on the Vp/Vs ratio model, consistent with the evidence that there is little correlation

Figure 5. Horizontal slices of (a–c) Vp, (d–f) Vs, and (g–i) Vp/Vs ratio in the upper crust at 2 km, in the middle crust at 10 km, and in the lower crust at 20 km depth. The thick gray lines show the Peninsular Range Compositional Boundary (Langenheim et al., 2004). Magenta lines in (i) and (h) represent cross sections shown in Figures 6 and 7. Regions with sparse data coverage have been masked out.
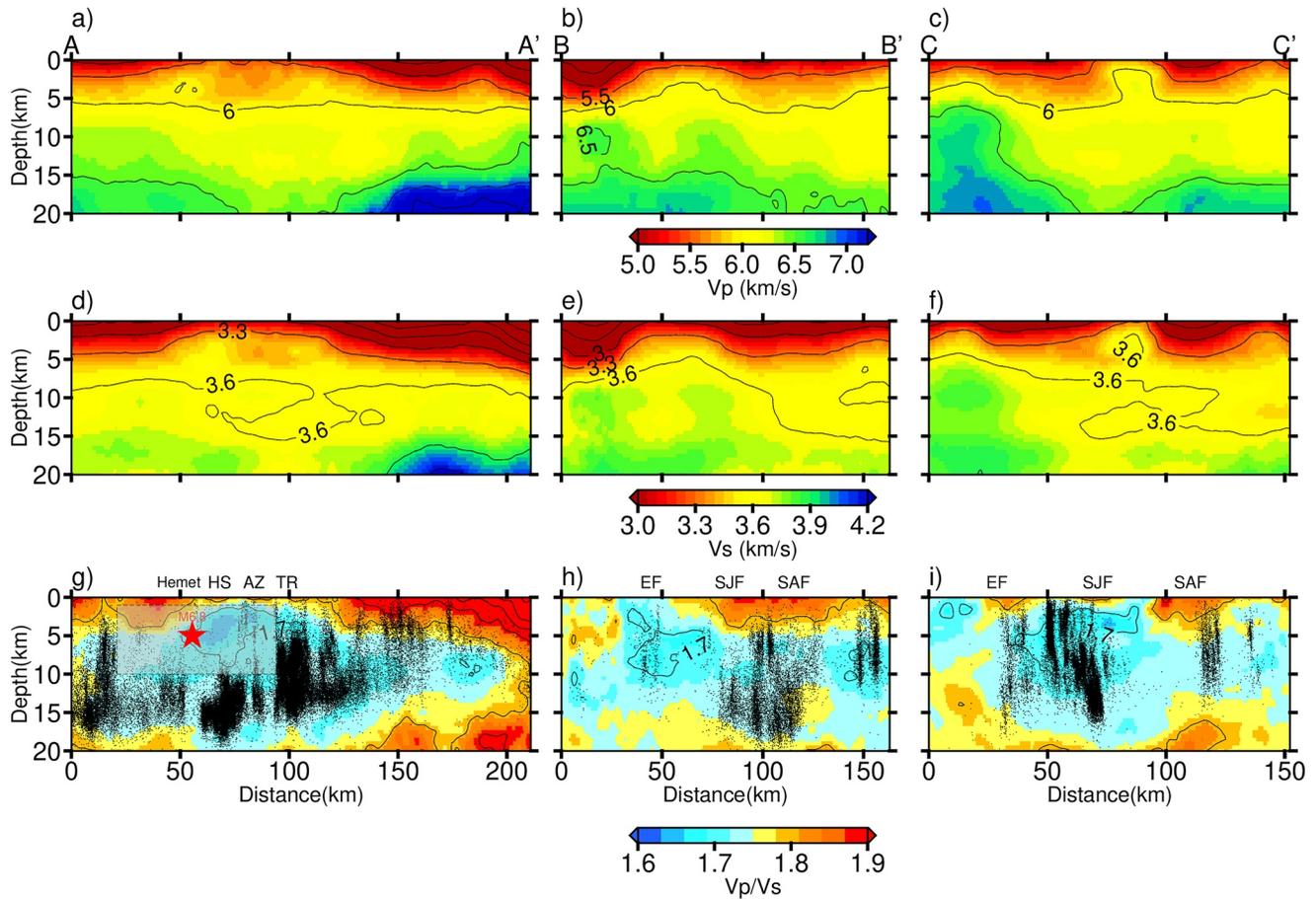
between felsic and mafic rock compositions and Poisson's ratio (Christensen, 1996). The regions around ST show high Vp and Vp/Vs ratios, but insignificant Vs anomalies. In the lower crust (about 20 km depth), the contrast across the PRCB is still clearly visible in the Vp model and is weakly visible in the Vs model; this is consistent with gravity and magnetic modeling (Langenheim et al., 2004). The region to the southwest of ST shows a very high Vp and Vp/Vs ratio, likely indicative of upwelling mantle material associated with rifting. This anomalous Vp/Vs ratio could also be seen in Share et al. (2021) but with a different interpretation of crustal weak zone given their relatively low Vp values. A belt of a NW-trending, low-velocity material in the Vp model correlates with the locations of declustered seismicity, indicating the ongoing rifting in Baja California may control the deformation along the East California Shear Zone (ECSZ) (Plattner et al., 2010) and might delineate the future location of the plate boundary (Ben-Zion & Zaliapin, 2019; Thatcher et al., 2016). The Vp/Vs model, although subjected to larger uncertainty (more on this in the discussion), generally shows elevated values (1.75–2.0) in the upper and lower crust and low to intermediate values (1.6–1.75) in the middle crust. This might be related to the depth dependence of brittle rock damage (fracture density), among other factors such as lithology, fracture density, water content, and partial melting. Owing to the incorporation of data from the intense seismicity of the 2019 Ridgecrest, CA, earthquake sequence, the resolution of our model in the Ridgecrest, CA, region is significantly greater than that of previous regional models. For example, the Vp and Vs at 2 km depth are similar to a local tomography model of White et al. (2021) for the Ridgecrest area and is more consistent with local geological features with high wavespeeds correlated with granodiorite surrounding low wavespeed alluvium, which is not clearly shown in other regional models (Figure S5 in Supporting Information S1).

An along-strike variation of Vp and Vs in the San Jacinto fault zone (SJFZ), with elevated Vp and Vs in the lower crust (depth >15 km) near the SE end, might be associated with mantle upwelling (Figure 6). The Anza and Trifurcation regions exhibit relatively low Vp of about 6.0 km/s and Vs of 3.6 km/s from 10 to 20 km depth in the middle to the lower crust. The low Vp, Vs, and high Vp/Vs ratio above 5 km correspond well with sedimentary material in the SW part of this cross section. Similar to Fang et al. (2019) and Lin and Shearer (2009), we also find that most of the seismicity is associated with normal to low Vp/Vs ratio, which Lin and Shearer (2009) suggested is evidence of water-filled cracks. Seismicity near the SJF clusters strongly, primarily in the Hot Springs and Trifurcation regions as in the local tomography study of Allam et al. (2014), and gradually shallows toward the SE, correlating with increasing Vp/Vs ratio beneath 15 km. The Vp and Vs contrasts across the SJF and Elsinore fault (EF) near the Hot Springs area are consistent with overall higher wavespeeds to the SW below 5 km. The wavespeed contrast across the EF flips polarity above 5 km, with lower wavespeeds to the SW which is associated with sedimentary materials in the Los Angeles basin. The Vp and Vs contrasts persist to the SE over a greater distance for EF than SJF. The San Andreas fault (SAF) does not exhibit strong cross-fault velocity contrasts, although analysis of fault zone head waves indicates a sharp wavespeed contrast along the southern SAF, with a reversal in the sense of wavespeed contrast across the SAF around San Gorgonio Pass (Share & Ben-Zion, 2016). A flower-shaped anomaly around the SAF with low Vp, Vs, and high Vp/Vs anomaly (Figures 6c, 6f and 6i) indicates a damage zone.

In the East California Shear Zone (ECSZ) and the Ridgecrest region, the structure becomes simpler with smaller lateral variation compared to the plate boundary region (Figure 7); however, there seems to be a low Vs layer between 10 and 15 km, which is not clearly shown in the Vp model, except in the Ridgecrest area. This low Vs layer, which is likely weak with reduced viscosity, may contribute to viscoelastic flow and could explain both horizontal and near-vertical displacement after the 1992 Landers earthquake, the extensional features observed in the Basin and Range province (Deng et al., 1998), relatively small fault spacing (Yang et al., 2020), and near-orthogonal strike-slip faulting in the ECSZ (Liang et al., 2021). Interestingly, most seismicity in these regions is above 10 km depth, directly above the low Vs layer. Unlike in other regions where most seismicity is associated with normal to low Vp/Vs ratio, in the Ridgecrest region, a significant amount of seismicity is distributed in regions with large (>1.75) Vp/Vs ratios (Figure 7).

3.3. Model Validation

Tomographic models provide valuable information for many topics when the derived results are accompanied by uncertainty estimates and are effectively validated. However, little attention has been given to effective and efficient techniques for doing so. The widely used checkerboard resolution tests, where an input model with a checkerboard pattern is used to generate synthetic traveltimes which are subsequently inverted using the same forward solver, can be misleading and reveal little about the true model resolution (Lévêque et al., 1993; Rawlinson &
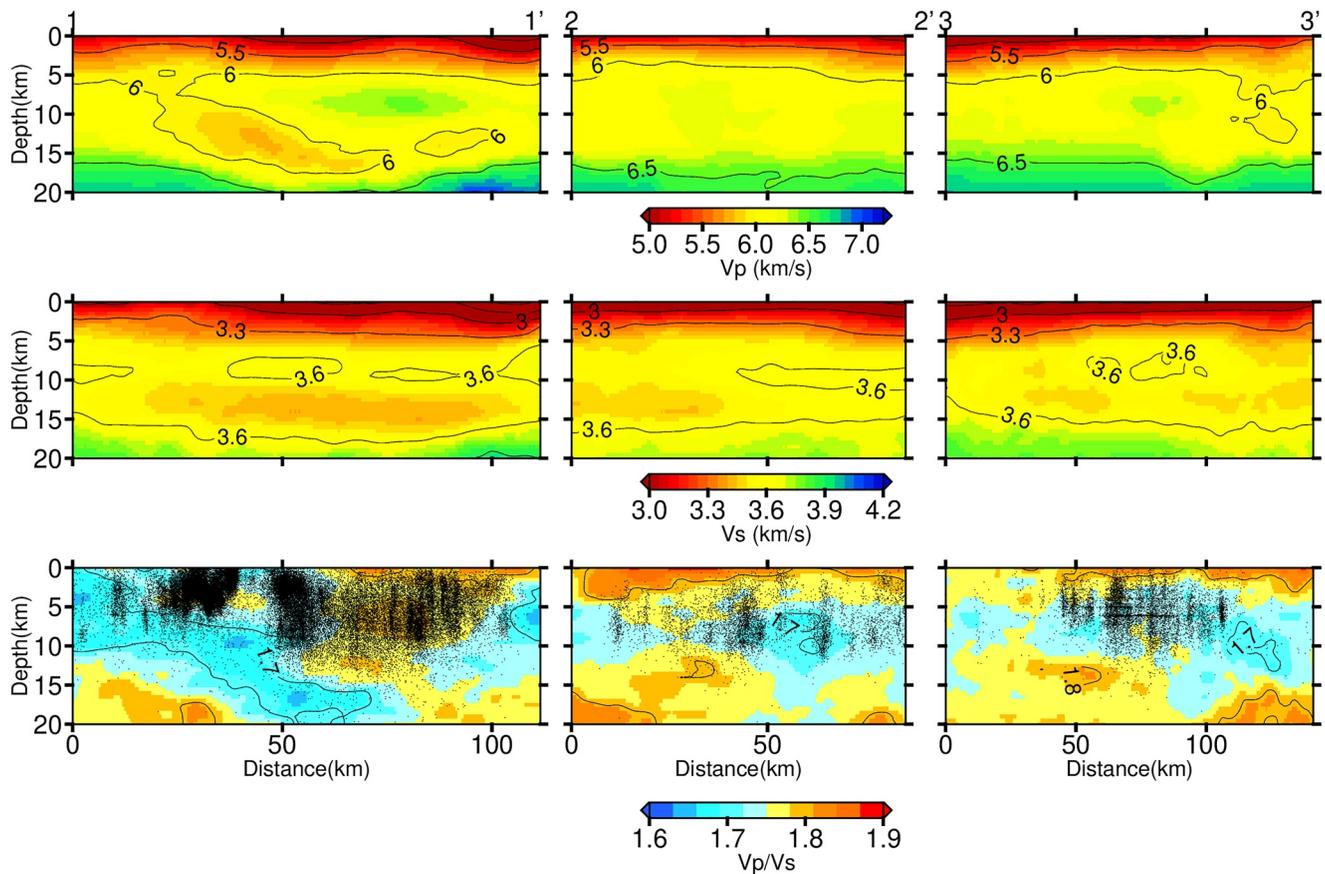
Figure 6. Cross sections of (a–c) Vp, (d–f) Vs, and (g–i) Vp/Vs ration in the plate boundary regions. The positions are shown in Figure 5i. Black dots in (g–i) indicate earthquakes within 10 km from the profiles. The red star in (g) represents the approximate location of the 1918 M6.8 earthquake (Townley, 1918), the shaded rectangular shows the potential rupture area for a future, large earthquake, see texts for more details. AZ, Anza; HS, Hot spring; TR, Trifurcation; The vertical exaggeration is about 1.8.

Spakman, 2016). Further, such synthetic tests do not account for observational errors in the data, which usually follow a non-Gaussian distribution. Considering these intrinsic drawbacks of checkerboard tests, we consider three alternative methods for validating the robustness of our models: (a) We inspect model uncertainty, which we obtain directly from our Poisson-Voronoi cells based tomography. (b) We compare the goodness of fit between observed waveforms and synthetic waveforms generated using our models with those generated using other available models. And (c) we test the robustness of model features against different starting models.

Estimates of model uncertainty arise naturally from our inversion method because we iteratively realize the inverse subproblem using randomly sampled subsets of redundant observations and randomized model parameterizations (Fang et al., 2020). Because the Vp/Vs model is derived by directly dividing Vp model parameters by Vs, we estimate uncertainty for the Vp/Vs model parameters using the same equation as White et al. (2021) (their Equation 4):

$$\sigma_{P/S} = \sqrt{\left(\frac{\partial}{\partial V_P}\frac{V_P}{V_S}\right)^2 \sigma_P^2 + \left(\frac{\partial}{\partial V_S}\frac{V_P}{V_S}\right)^2 \sigma_S^2}. \tag{2}$$
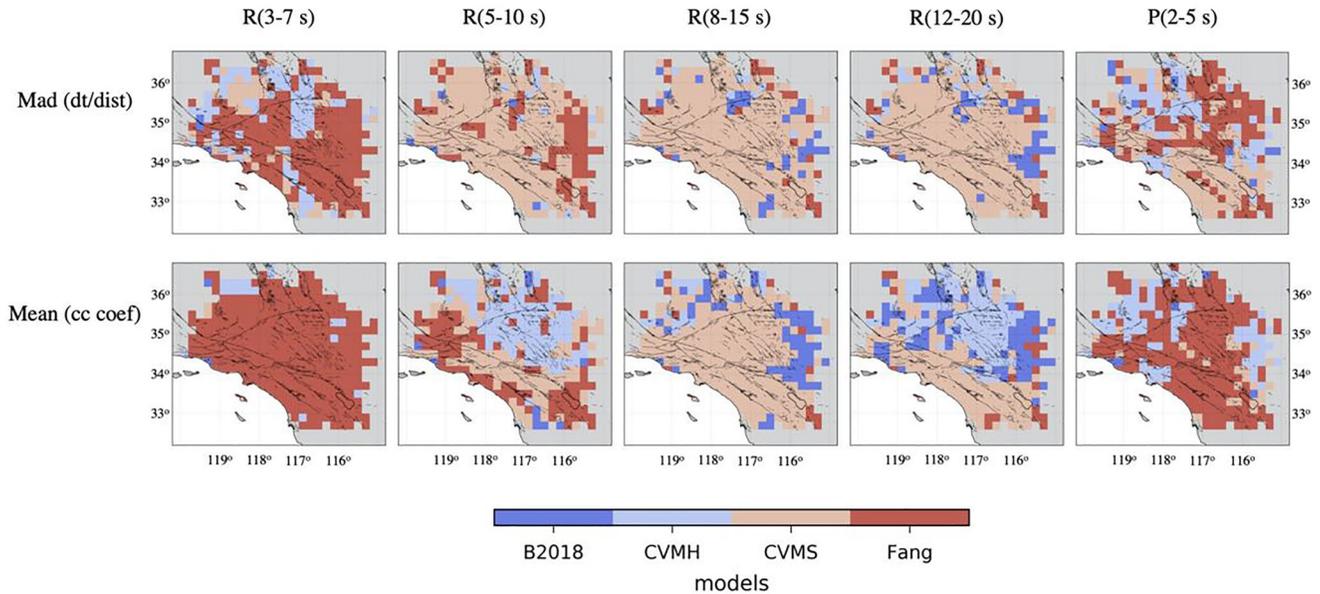
Model uncertainty estimates for both Vp and Vs (Figure S6 in Supporting Information S1) show low uncertainty in regions with dense data coverage, for example, at intermediate depths (around 10 km), but increases slightly at shallower and deeper depths. The uncertainty associated with the Vp/Vs model is relatively large compared to that of Vp and Vs models, which is expected for propagating error from the Vp and Vs models.

Figure 7. Same as Figure 6 but for cross sections in the ECSZ and the Ridgecrest region. Positions of the cross sections are shown in Figure 5h.

We further validate our models and three other regional models for southern California—(a) CVM-S4.26 (Lee et al., 2014), (b) CVM-H15.1 (Shaw et al., 2015), and (c) the model from Berg et al. (2018) with full waveform simulations following the workflow proposed by Lu and Ben-Zion (2022). For each set of examined models, we simulated waveforms (with period ≥ 2 s) for 48 virtual seismic noise sources and 44 earthquake events using 3D viscoelastic simulations. The synthetic waveforms are compared with observations of noise cross-correlation and earthquake datasets (Figure S7 in Supporting Information S1). The goodness of fit is quantified, at different period bands, for different seismic phases, by measuring the distance-weighted travel time delays and normalized zero-lag cross-correlations between synthetics and observations. The two types of measurements are regionalized to evaluate the spatial variation of model quality in terms of travel time difference and waveform similarity. A detailed description of this model validation procedure is beyond the scope of the current discussion and is comprehensively reported in Lu and Ben-Zion (2022). Here, we focus on the comparison of regionalized model quality among the four examined models. Figure 8 shows the model exhibiting the best regional model performance regarding P and Rayleigh waves in multiple period bands. We find that our model outperforms the other regional models for both P and Rayleigh waves at short periods of less than 5 s, which we expect because our models are derived from a large number of high-frequency body-wave observations. The goodness of fit, however, degrades for periods longer than about 7 s for Rayleigh waves, indicating less constraint than the other tested models in the deep crust. We speculate that incorporating long-period surface wave dispersion data, such as those used in Berg et al. (2018), and short-period H/V data (Muir & Tsai, 2017), or merging models from different studies could further improve the data fitting.

Finally, we test the dependence of our final models on the initial models by comparing results obtained from different initial models, including the SCEC HK1D (Hauksson, 2000) and an average, 1D model extracted from Berg et al. (2018) (Figure S8 in Supporting Information S1), and we find that general features of the relocated event distributions (Figure S9 in Supporting Information S1) and wavespeed models (Figure S10 in Supporting

Figure 8. Model validation comparison among the B2018 model (Berg et al., 2018) (blue), the community model CVMH-15.1 (Shaw et al., 2015) (light blue), the CVMS-4.26 (Lee et al., 2014) (light brown), and models from this study (red) using waveform simulation. Different colors in each panel show the best regional performance based on criteria of travel time delays (top row) and waveform similarity (bottom row). Mad (dt/dist) refers to the mean absolute deviation value of the distance-weighted travel time delay measurements; Mean (cc coef) indicates the mean value of the normalized zero-lag cross-correlation measurements; P and R stand for P-waves and Rayleigh waves, respectively.
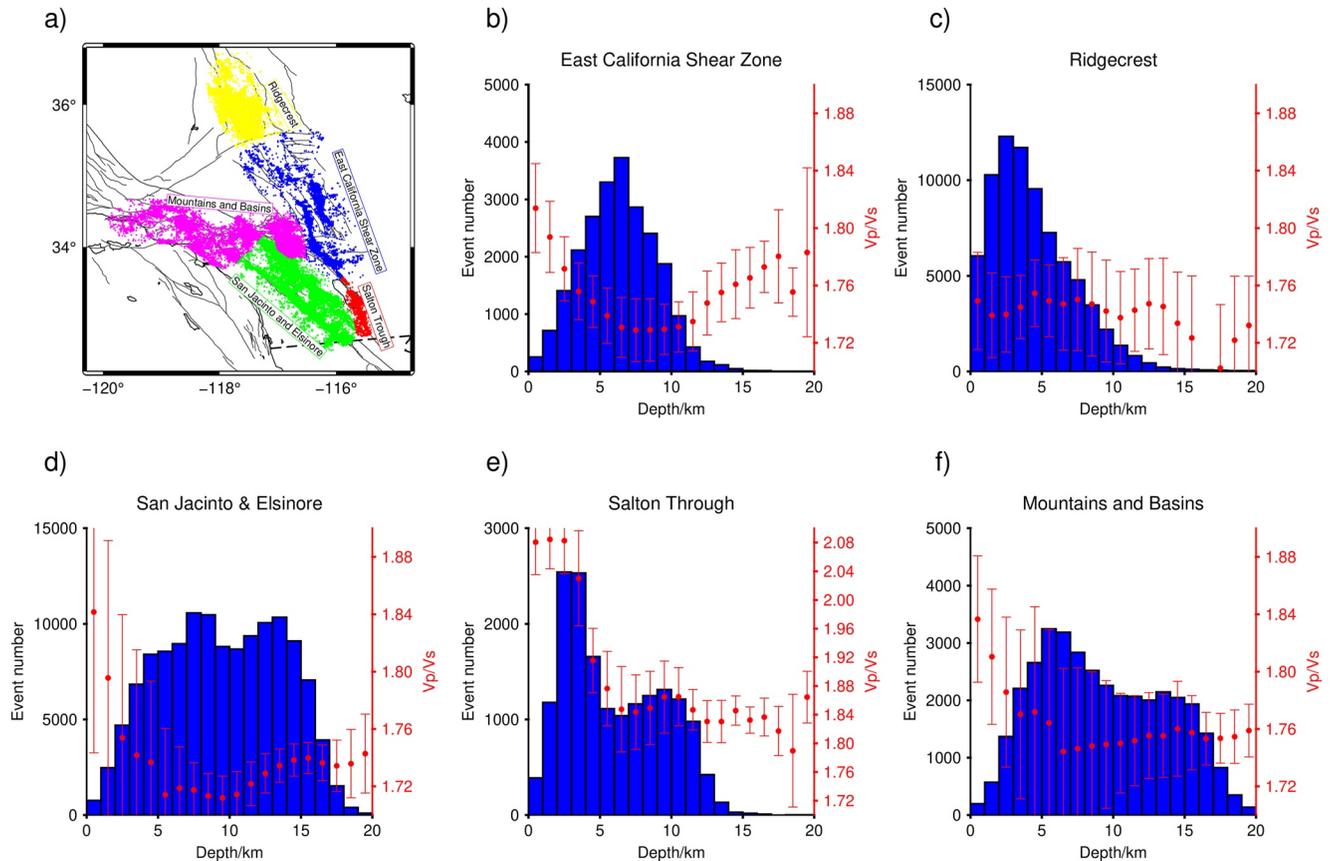
Information S1) are qualitatively similar. The independence of the model features that we interpret below on the initial model supports the robustness of our model interpretations.

4. Discussion and Conclusions

We recompile 20 years of P- and S-wave arrival-time data for southern California comprising over 0.3 million event locations and high quality analysts-reviewed phase arrival picks (about 7.4 million and 4.2 million P- and S-wave arrivals, respectively) from the SCEDC, which we augment with more than 2.9 million additional S-wave arrivals from an automated picking algorithm. Using these data and a parsimonious Poisson-Voronoi cell tomography method, we derive new Vp, Vs, and Vp/Vs ratio models and iteratively update the models and relocate the SoCal earthquake catalog using the updated models and a fully 3D, non-linear, global optimization algorithm. We validate our new models using multiple techniques, including comparisons between synthetic and observed waveforms from events not used for the tomographic inversion. Observed tomographic features correlate strongly with the surface geology, as shown in Section 3. This holds not only for the Vp and Vs models but also for the Vp/Vs ratios, despite having larger uncertainties than the individual Vp and Vs models. The derived wavespeed models and relocated seismicity help to clarify several aspects of fault mechanics and regional tectonics, which we discuss below.

Large values in our Vp/Vs ratio model correlate with major basins in southern California better than both the CVM-S4.26 and CVM-H15.1 community models (Figure S11 in Supporting Information S1). The correlations between Vp and Vs models and geology in southern California have been extensively discussed elsewhere. We therefore primarily focus below on the Vp/Vs ratios, which imposes stronger constraints on crustal properties, such as lithology, crack density, and fluid content than Vp and Vs models do alone, and the relocated seismicity. We inspect the overall relations between the Vp/Vs ratios and spatial seismicity patterns by focusing on general features and robust statistics, such as average 1D depth profiles. Although care must be taken when interpreting absolute Vp/Vs values, the relative values are less prone to errors, and the preceding comparisons of patterns supports the interpretation that follows.
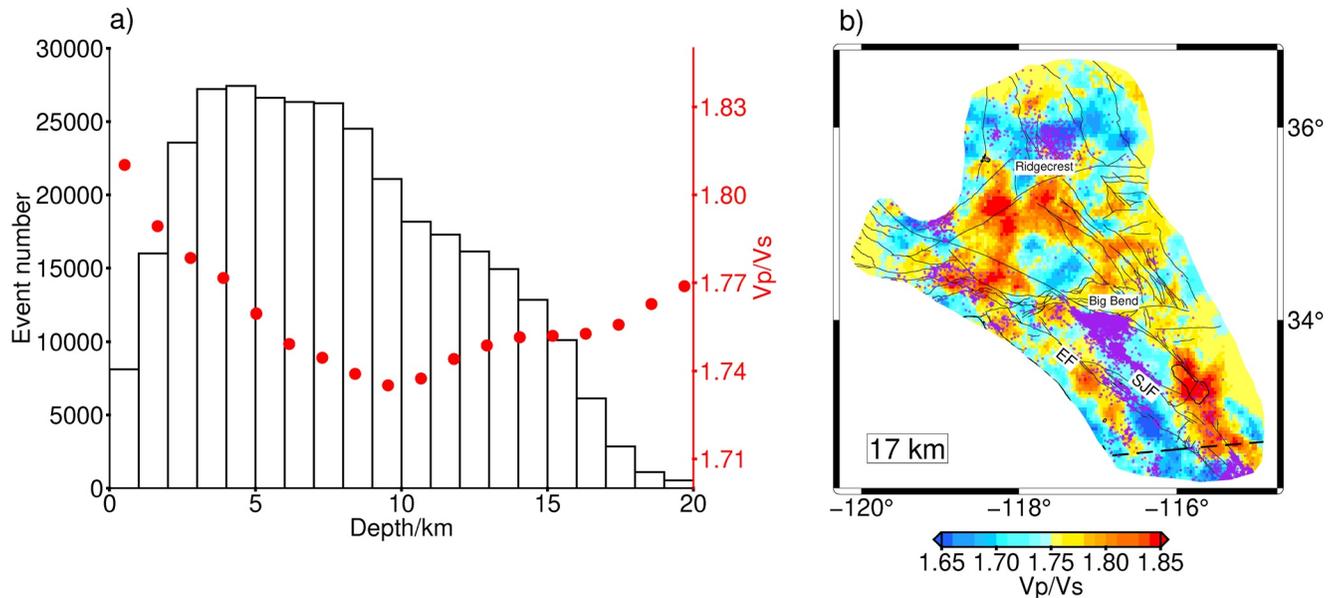
First, we examine the association between the depth distribution of seismicity and Vp/Vs ratios in different tectonic units of southern California (e.g., Ben-Zion & Zaliapin, 2020; Eymold & Jordan, 2019). We observe

Figure 9. Analysis of the seismicity and Vp/Vs ratio in different regions. (a) Event distribution in the Ridgecrest (yellow), East California Shear Zone (blue), Salton Trough (red), Transverse Range region (magenta), and the San Jacinto and Elsinore fault region (green). (b–f) The depth distribution of seismicity and their associated Vp/Vs ratio in different regions. The red dots indicate the mean Vp/Vs and the vertical bars are the standard deviations.

relatively few shallow events (above 3 km depth), most of which are associated with a relatively high Vp/Vs ratio (Figure 9). The Ridgecrest, CA, region manifests low Vp/Vs and increased seismicity in the shallow crust. Most events in southern California occur between 3 and 15 km depth with intermediate to low Vp/Vs ratio, except in the ST, where depth-averaged Vp/Vs is elevated throughout the seismogenic crust. There are, however, fewer events there compared to other seismically active regions. Unlike shallow events, which are associated with Vp/Vs ratios >1.77, most events occur in regions with low to intermediate Vp/Vs values. The seismicity in ECSZ and Ridgecrest is mostly above 10 km, which may indicate decreased brittle-to-ductile transition depth in these regions, as also suggested by the low Vs layers observed in Figure 7.

The depth-averaged Vp/Vs ratio in southern California decreases with increasing depth from about 1.8 at the surface to a minimum of 1.74 at 10 km depth. Below 10 km, it gradually increases to about 1.77 at 20 km depth (Figure 10a). The high Vp/Vs values at shallow depths are consistent with intensive rock damage around fault zones and basins associated with unconsolidated materials and fluids. Low Vp/Vs ratio at round 10 km may be related with diminished rock damage, dry rocks, or fluids-filled cracks with large aspect ratio (Lin & Shearer, 2009; Shearer, 1988). This 1D Vp/Vs profile correlates negatively with the expected rock strength profile in the top 10 km, at which depth Vp/Vs reaches a minimum. The seismic event intensity correlates negatively with the average Vp/Vs profile over the entire depth range, but peaks at a shallower depth (around 5 km). This probably implies that additional properties and processes beyond rock strength, as indicated by the depth averaged Vp/Vs ratio, influence earthquake nucleation, such as decreasing fault zone width with depth (e.g., Hillers et al., 2006) and stress/strength heterogeneities (e.g., Ben-Zion, 2008). Most deep seismicity (i.e., below 15 km) is located in regions of Vp/Vs ratio lower than 1.75 (Figure 10b), and occurs predominantly around the Ridgecrest, CA, area, the Big Bend region, and along the SJF. The intensity of deep seismic activity decreases dramatically at the SE end of the SJF where the Vp/Vs ratio increases. A similar pattern manifests in the EF where

Figure 10. (a) Depth distribution of all events and the average Vp/Vs ratio at each depth (red dots). (b) Distribution of deep seismicity (purple dots) with depths larger than 15 km with the background of Vp/Vs ratio at 17 km depth.

deep seismicity coincides with relatively low Vp/Vs ratio. The correlation between deep seismicity and Vp/Vs ratios may reflect spatial variability of the brittle-to-ductile transition depth, which is important for various aspects of crustal deformation and seismic hazard.

Tight, fault-normal, spatial clustering of events observed in the relocated catalog helps constrain subsurface fault-zone geometry, and, tight, spatial clustering of events in cross sections parallel to the primary trend of fault zone (Figures 6 and 7) might indicate hierarchical cross-cutting faults, which are common in complex fault regions. Prominent examples of such cross-cutting features include the 1987 Superstition Hills earthquake sequence (Hudnut et al., 1989) and the 2019 Ridgecrest earthquake sequence (Ross et al., 2019).

Seismicity at the base of the seismogenic zone in the core SJFZ is spatiotemporally diffuse, which likely reflects the transition between brittlely deforming crust above and ductilely deforming crust below (e.g., White et al., 2019). A large, aseismic region, with a lateral extent of about 70 km, NW of the Hot Springs Area in the SJFZ (Figure 6g), hosted a M6.8 earthquake in 1918 (Townley, 1918). Assuming that the SJF accommodates half of the plate motion (about 20 mm/year) (Fialko, 2006), and that the fault is fully locked over a depth of 10 km, we estimate a slip deficit of about 2 m over this 70 km fault segment. Using these values to estimate the cumulative seismic potency (rupture area times slip) since 1918, and converting the potency to magnitude using the quadratic scaling relation of Ben-Zion and Zhu (2002), suggest that this fault segment has enough stored strain energy to produce another M6.8 or larger earthquake.

The derived wavespeed models can be further improved by incorporating long-period surface wave dispersion data (e.g., Berg et al., 2018) and short-period H/V data (e.g., Muir & Tsai, 2017). Alternatively, different models could be merged using validation tests as in Figure 8 to weight each model based on its performance. It is also worth noting that, although we did not use differential arrival time measurements, the relocated catalog exhibits tighter spatial clustering near major faults, as is commonly seen in catalogs derived using double-difference relocation techniques (e.g., Hauksson & Shearer, 2005; Lin et al., 2007; Trugman & Shearer, 2017). Because the individual event location algorithm using an improved 3D model provides more accurate absolute locations, we speculate that combining our relocated events with a relative relocation technique would further improve the event locations and thus better characterize subsurface fault-zone geometry. Such improvements to the wavespeed models and locations may be the subject of follow up studies.

Data Availability Statement

The initial catalog, P- and S-wave arrival times, and raw data used for automatic picking for the CI networks and can be accessed through Southern California Earthquake Data Center. The fault traces were downloaded from the SCEC Community Fault Model (https://www.scec.org/research/cfm, last accessed 1 June 2021). The wavespeed models and relocated seismicity can be downloaded from https://data.mendeley.com/datasets/4rdhjsc54p. The PyVoroTomo code used in this work can be obtained at https://github.com/HongjianFang/PyVoroTomo or https://doi.org/10.5281/zenodo.6015701 (Fang, 2022). All figures were created using GMT plotting software (Wessel et al., 2019).

References

Akaike, H. (1974). A new look at the statistical model identification. *IEEE Transactions on Automatic Control*, *19*(6), 716–723. https://doi.org/10.1109/TAC.1974.1100705

Allam, A., & Ben-Zion, Y. (2012). Seismic velocity structures in the southern California plate-boundary environment from double-difference tomography. *Geophysical Journal International*, *190*(2), 1181–1196. https://doi.org/10.1111/j.1365-246x.2012.05544.x

Allam, A., Ben-Zion, Y., Kurzon, I., & Vernon, F. (2014). Seismic velocity structure in the Hot Springs and Trifurcation areas of the San Jacinto fault zone, California, from double-difference tomography. *Geophysical Journal International*, *198*(2), 978–999. https://doi.org/10.1093/gji/ggu176

Barak, S., Klemperer, S. L., & Lawrence, J. F. (2015). San Andreas Fault dip, Peninsular ranges mafic lower crust and partial melt in the Salton Trough, Southern California, from ambient-noise tomography. *Geochemistry, Geophysics, Geosystems*, *16*(11), 3946–3972. https://doi.org/10.1002/2015GC005970

Ben-Zion, Y. (2008). Collective behavior of earthquakes and faults: Continuum-discrete transitions, progressive evolutionary changes, and different dynamic regimes. *Reviews of Geophysics*, *46*(4), RG4006. https://doi.org/10.1029/2008rg000260

Ben-Zion, Y., & Zaliapin, I. (2019). Spatial variations of rock damage production by earthquakes in southern California. *Earth and Planetary Science Letters*, *512*, 184–193. https://doi.org/10.1016/j.epsl.2019.02.006

Ben-Zion, Y., & Zaliapin, I. (2020). Localization and coalescence of seismicity before large earthquakes. *Geophysical Journal International*, *223*(1), 561–583. https://doi.org/10.1093/gji/ggaa315

Ben-Zion, Y., & Zhu, L. (2002). Potency-magnitude scaling relations for southern California earthquakes with $1.0 < M_L < 7.0$. *Geophysical Journal International*, *148*(3), F1–F5. https://doi.org/10.1046/j.1365-246x.2002.01637.x

Berg, E. M., Lin, F., Allam, A., Qiu, H., Shen, W., & Ben-Zion, Y. (2018). Tomography of Southern California via Bayesian joint inversion of Rayleigh wave ellipticity and phase velocity from ambient noise cross-correlations. *Journal of Geophysical Research: Solid Earth*, *123*(11), 9933–9949. https://doi.org/10.1029/2018jb016269

Berg, E. M., Lin, F., Schulte-Pelkum, V., Allam, A., Qiu, H., & Gkogkas, K. (2021). Shallow crustal shear velocity and Vp/Vs across Southern California: Joint inversion of short-period Rayleigh wave ellipticity, phase velocity, and teleseismic receiver functions. *Geophysical Research Letters*, *48*(15). https://doi.org/10.1029/2021gl092626

Blackwell, D., & Richards, M. (2004). *Geothermal map of north America: American association of petroleum geologists*. scale (1: 6,500,000).

Christensen, N. I. (1996). Poisson's ratio and crustal seismology. *Journal of Geophysical Research*, *101*(B2), 3139–3156. (1978–2012). https://doi.org/10.1029/95jb03446

Deng, J., Gurnis, M., Kanamori, H., & Hauksson, E. (1998). Viscoelastic flow in the lower crust after the 1992 Landers, California, earthquake. *Science*, *282*(5394), 1689–1692. https://doi.org/10.1126/science.282.5394.1689

Eymold, W. K., & Jordan, T. H. (2019). Tectonic regionalization of the southern California crust from tomographic cluster analysis. *Journal of Geophysical Research: Solid Earth*, *124*(11), 11840–11865. https://doi.org/10.1029/2019jb018423

Fang, H. (2022). *HongjianFang/PyVoroTomo: Seismic traveltime tomography for southern California using 20 years of data*. https://doi.org/10.5281/zenodo.6015701

Fang, H., van der Hilst, R. D., de Hoop, M. V., Kothari, K., Gupta, S., & Dokmanić, I. (2020). Parsimonious seismic tomography with Poisson Voronoi projections: Methodology and validation. *Seismological Research Letters*, *91*(1), 343–355. https://doi.org/10.1785/0220190141

Fang, H., Yao, H., Zhang, H., Thurber, C., Ben-Zion, Y., & van der Hilst, R. D. (2019). Vp/Vs tomography in the southern California plate boundary region using body and surface wave traveltime data. *Geophysical Journal International*, *216*(1), 609–620. https://doi.org/10.1093/gji/ggy458

Fang, H., Zhang, H., Yao, H., Allam, A., Zigone, D., Ben-Zion, Y., et al. (2016). A new algorithm for three-dimensional joint inversion of body wave and surface wave data and its application to the Southern California plate boundary region. *Journal of Geophysical Research: Solid Earth*, *121*(5), 3557–3569. https://doi.org/10.1002/2015JB012702

Fialko, Y. (2006). Interseismic strain accumulation and the earthquake potential on the southern San Andreas fault system. *Nature*, *441*(7096), 968–971. https://doi.org/10.1038/nature04797

Han, L., Hole, J. A., Stock, J. M., Fuis, G. S., Kell, A., Driscoll, N. W., et al. (2016). Continental rupture and the creation of new crust in the Salton Trough rift, southern California and northern Mexico: Results from the Salton seismic imaging project. *Journal of Geophysical Research: Solid Earth*, *121*(10), 7469–7489. https://doi.org/10.1002/2016jb013139

Hauksson, E. (2000). Crustal structure and seismicity distribution adjacent to the Pacific and North America plate boundary in southern California. *Journal of Geophysical Research*, *105*(B6), 13875–13903. https://doi.org/10.1029/2000jb900016

Hauksson, E., & Shearer, P. (2005). Southern California hypocenter relocation with waveform cross-correlation, part 1: Results using the double-difference method. *Bulletin of the Seismological Society of America*, *95*(3), 896–903. https://doi.org/10.1785/0120040167

Hauksson, E., Yang, W., & Shearer, P. M. (2012). Waveform relocated earthquake catalog for southern California (1981 to June 2011). *Bulletin of the Seismological Society of America*, *102*(5), 2239–2244. https://doi.org/10.1785/0120120010

Hillers, G., Ben-Zion, Y., & Mai, P. (2006). Seismicity on a fault controlled by rate-and state-dependent friction with spatial variations of the critical slip distance. *Journal of Geophysical Research*, *111*(B1), B01403. https://doi.org/10.1029/2005jb003859

Hudnut, K. W., Seeber, L., & Pacheco, J. (1989). Cross-fault triggering in the November 1987 Superstition Hills earthquake sequence, southern California. *Geophysical Research Letters*, *16*(2), 199–202. https://doi.org/10.1029/gl016i002p00199

Kennett, B., Widiyantoro, S., & van der Hilst, R. (1998). Joint seismic tomography for bulk sound and shear wave speed in the Earth's mantle. *Journal of Geophysical Research*, *103*(B6), 12469–12493. https://doi.org/10.1029/98jb00150

Langenheim, V., Jachens, R., Morton, D., Kistler, R., & Matti, J. (2004). Geophysical and isotopic mapping of preexisting crustal structures that influenced the location and development of the San Jacinto fault zone, southern California. *The Geological Society of America Bulletin*, *116*(9–10), 1143–1157. https://doi.org/10.1130/B25277.1

Lee, E., Chen, P., Jordan, T. H., Maechling, P. B., Denolle, M. A., & Beroza, G. C. (2014). Full-3-D tomography for crustal structure in Southern California based on the scattering-integral and the adjoint-wavefield methods. *Journal of Geophysical Research: Solid Earth*, *119*(8), 6421–6451. https://doi.org/10.1002/2014JB011346

Lévêque, J.-J., Rivera, L., & Wittlinger, G. (1993). On the use of the checker-board test to assess the resolution of tomographic inversions. *Geophysical Journal International*, *115*(1), 313–318. https://doi.org/10.1111/j.1365-246x.1993.tb05605.x

Liang, C., Ampuero, J.-P., & Pino Muñoz, D. (2021). Deep ductile shear zone facilitates near-orthogonal strike-slip faulting in a thin brittle lithosphere. *Geophysical Research Letters*, *48*(2), e2020GL090744. https://doi.org/10.1029/2020gl090744

Lin, G., & Shearer, P. M. (2009). Evidence for water-filled cracks in earthquake source regions. *Geophysical Research Letters*, *36*(17), L17315. https://doi.org/10.1029/2009gl039098

Lin, G., Shearer, P. M., Hauksson, E., & Thurber, C. H. (2007). A three-dimensional crustal seismic velocity model for southern California from a composite event method. *Journal of Geophysical Research*, *112*(B11), B11306. (1978–2012). https://doi.org/10.1029/2007JB004977

Lu, Y., & Ben-Zion, Y. (2022). Validation of seismic velocity models in southern California with full-waveform simulations. *Geophysical Journal International*, *229*(2), 1232–1254. https://doi.org/10.1093/gji/ggab534

Muir, J. B., & Tsai, V. C. (2017). Rayleigh-wave H/V via noise cross correlation in southern California. *Bulletin of the Seismological Society of America*, *107*(5), 2021–2027. https://doi.org/10.1785/0120170051

Ozakin, Y., & Ben-Zion, Y. (2015). Systematic receiver function analysis of the Moho geometry in the southern California plate-boundary region. *Pure and Applied Geophysics*, *172*(5), 1167–1184. https://doi.org/10.1007/s00024-014-0924-6

Plattner, C., Malservisi, R., Furlong, K., & Govers, R. (2010). Development of the Eastern California Shear Zone—Walker Lane belt: The effects of microplate motion and pre-existing weakness in the Basin and Range. *Tectonophysics*, *485*(1–4), 78–84. https://doi.org/10.1016/j.tecto.2009.11.021

Qiu, H., Lin, F.-C., & Ben-Zion, Y. (2019). Eikonal tomography of the Southern California plate boundary region. *Journal of Geophysical Research: Solid Earth*, *124*(9), 9755–9779. https://doi.org/10.1029/2019jb017806

Rawlinson, N., & Spakman, W. (2016). On the use of sensitivity tests in seismic tomography. *Geophysical Journal International*, *205*(2), 1221–1243. https://doi.org/10.1093/gji/ggw084

Ross, Z. E., Idini, B., Jia, Z., Stephenson, O. L., Zhong, M., Wang, X., et al. (2019). Hierarchical interlocked orthogonal faulting in the 2019 Ridgecrest earthquake sequence. *Science*, *366*(6463), 346–351. https://doi.org/10.1126/science.aaz0109

Sambridge, M., & Guðmundsson, Ó. (1998). Tomographic systems of equations with irregular cells. *Journal of Geophysical Research*, *103*(B1), 773–781. https://doi.org/10.1029/97jb02602

Share, P.-E., & Ben-Zion, Y. (2016). Bimaterial interfaces in the south San Andreas fault with opposite velocity contrasts NW and SE from San Gorgonio Pass. *Geophysical Research Letters*, *43*(20), 10680–10687. https://doi.org/10.1002/2016gl070774

Share, P.-E., Castro, R., Vidal-Villegas, J., Mendoza, L., & Ben-Zion, Y. (2021). High-resolution seismic imaging of the plate boundary in northern Baja California and southern California using double-pair double-difference tomography. *Earth and Planetary Science Letters*, *568*, 117004. https://doi.org/10.1016/j.epsl.2021.117004

Shaw, J. H., Plesch, A., Tape, C., Suess, P. M., Jordan, T. H., Ely, G., et al. (2015). Unified structural representation of the southern California crust and upper mantle. *Earth and Planetary Science Letters*, *415*, 1–15. https://doi.org/10.1016/j.epsl.2015.01.016

Shearer, P. M. (1988). Cracked media, Poisson's ratio and the structure of the upper oceanic crust. *Geophysical Journal*, *92*(2), 357–362. https://doi.org/10.1111/j.1365-246x.1988.tb01149.x

Simon, J. D., Simons, F. J., & Nolet, G. (2020). Multiscale estimation of event arrival times and their uncertainties in hydroacoustic records from autonomous oceanic floats. *Bulletin of the Seismological Society of America*, *110*(3), 970–997. https://doi.org/10.1785/0120190173

Southern California Earthquake Center. (2013). Southern California earthquake center [Dataset]. SCEDC. https://doi.org/10.7909/C3WD3xH1

Storn, R., & Price, K. (1997). Differential evolution–a simple and efficient heuristic for global optimization over continuous spaces. *Journal of Global Optimization*, *11*(4), 341–359. https://doi.org/10.1023/a:1008202821328

Tape, C., Liu, Q., Maggi, A., & Tromp, J. (2009). Adjoint tomography of the Southern California crust. *Science*, *325*(5943), 988–992. https://doi.org/10.1126/science.1175298

Tape, C., Liu, Q., Maggi, A., & Tromp, J. (2010). Seismic tomography of the southern California crust based on spectral-element and adjoint methods. *Geophysical Journal International*, *180*(1), 433–462. https://doi.org/10.1111/j.1365-246x.2009.04429.x

Thatcher, W., Savage, J. C., & Simpson, R. W. (2016). The Eastern California Shear Zone as the northward extension of the southern San Andreas Fault. *Journal of Geophysical Research: Solid Earth*, *121*(4), 2904–2914. https://doi.org/10.1002/2015jb012678

Tong, P. (2021). Adjoint-state equation traveltime tomography: Eikonal equation-based methods and application to the Anza area in southern California. *Journal of Geophysical Research: Solid Earth*, *126*(5), e2021JB021818. https://doi.org/10.1029/2021jb021818

Townley, S. D. (1918). The San Jacinto earthquake of April 21, 1918. *Bulletin of the Seismological Society of America*, *8*(2–3), 45–62. https://doi.org/10.1785/bssa0080020045

Trugman, D. T., & Shearer, P. M. (2017). GrowClust: A hierarchical clustering algorithm for relative earthquake relocation, with application to the Spanish Springs and Sheldon, Nevada, earthquake sequences. *Seismological Research Letters*, *88*(2A), 379–391. https://doi.org/10.1785/0220160188

Wang, K., Yang, Y., Basini, P., Tong, P., Tape, C., & Liu, Q. (2018). Refined crustal and uppermost mantle structure of southern California by ambient noise adjoint tomography. *Geophysical Journal International*, *215*(2), 844–863. https://doi.org/10.1093/gji/ggy312

Wessel, P., Luis, J., Uieda, L., Scharroo, R., Wobbe, F., Smith, W., & Tian, D. (2019). The generic mapping tools version 6. *Geochemistry, Geophysics, Geosystems*, *20*(11), 5556–5564. https://doi.org/10.1029/2019gc008515

White, M. C., Ben-Zion, Y., & Vernon, F. L. (2019). A detailed earthquake catalog for the San Jacinto fault-zone region in Southern California. *Journal of Geophysical Research: Solid Earth*, *124*(7), 6908–6930. https://doi.org/10.1029/2019jb017641

White, M. C. A., Fang, H., Catchings, R. D., Goldman, M. R., Steidl, J. H., & Ben-Zion, Y. (2021). Detailed traveltime tomography and seismic catalog around the 2019 Mw 7.1 Ridgecrest, California, earthquake using dense rapid-response seismic data. *Geophysical Journal International*, *227*(1), 204–227. https://doi.org/10.1093/gji/ggab224

White, M. C., Fang, H., Nakata, N., & Ben-Zion, Y. (2020). PyKonal: A Python package for solving the Eikonal equation in spherical and cartesian coordinates using the fast marching method. *Seismological Research Letters*, *91*(4), 2378–2389. https://doi.org/10.1785/0220190318

Xiong, N., Qiu, H., & Niu, F. (2021). Data-driven velocity model evaluation using K-means clustering. *Geophysical Research Letters*, *48*(23). https://doi.org/10.1029/2021gl096040

Yang, H., Moresi, L. N., & Quigley, M. (2020). Fault spacing in continental strike-slip shear zones. *Earth and Planetary Science Letters*, *530*, 115906. https://doi.org/10.1016/j.epsl.2019.115906

Zaliapin, I., & Ben-Zion, Y. (2013). Earthquake clusters in southern California I: Identification and stability. *Journal of Geophysical Research: Solid Earth*, *118*(6), 2847–2864. https://doi.org/10.1002/jgrb.50179

Zaliapin, I., & Ben-Zion, Y. (2021). Perspectives on clustering and declustering of earthquakes. *Seismological Research Letters*, *93*(1), 386–401. https://doi.org/10.1785/0220210127

Zhu, L., & Kanamori, H. (2000). Moho depth variation in southern California from teleseismic receiver functions. *Journal of Geophysical Research*, *105*(B2), 2969–2980. (1978–2012). https://doi.org/10.1029/1999JB900322

Zigone, D., Ben-Zion, Y., Campillo, M., & Roux, P. (2015). Seismic tomography of the Southern California plate boundary region from noise-based Rayleigh and Love waves. *Pure and Applied Geophysics*, *172*(5), 1007–1032. https://doi.org/10.1007/s00024-014-0872-1